Nuclearity and Host Effects of Carbon-Supported Platinum Catalysts for Dibromomethane Hydrodebromination

*Ali J. Saadun, Selina K. Kaiser, Andrea Ruiz-Ferrando, Sergio Pablo-García, Simon Büchele, Edvin Fako, Núria López, and Javier Pérez-Ramírez**

The identification of the active sites and the derivation of structure-performance relationships are central for the development of high-performance heterogeneous catalysts. Here, a platform of platinum nanostructures, ranging from single atoms to nanoparticles of ≈4 nm supported on activated- and N-doped carbon (AC and NC), is employed to systematically assess nuclearity and host effects on the activity, selectivity, and stability in dibromomethane hydrodebromination, a key step in bromine-mediated methane functionalization processes. For this purpose, catalytic evaluation is coupled to in-depth characterization, kinetic analysis, and mechanistic studies based on density functional theory. Remarkably, the single atom catalysts achieve exceptional selectivity toward CH_3Br (up to 98%) when compared to nanoparticles and any previously reported system. Furthermore, the results reveal unparalleled specific activity over 1.3–2.3 nm-sized platinum nanoparticles, which also exhibit the highest stability. Additionally, host effects are found to markedly affect the catalytic performance. Specifically, on NC, the activity and CH_3Br selectivity are enhanced, but significant fouling occurs. On the other hand, AC-supported platinum nanostructures deactivate due to sintering and bromination. Simulations and kinetic fingerprints demonstrate that the observed reactivity patterns are governed by the H_2 dissociation abilities of the catalysts and the availability of surface H-atoms.

1. Introduction

The development of heterogeneous metal-based catalysts that integrate a high density of active, selective, and stable ensembles, granting efficient turnover and prolonged lifetimes, is one of the main targets in catalysis science, often driven by increasing societal demands and environmental challenges.[1] This goal could be approached by engineering both the geometry and the electronic properties of the active phase at the nanoscale.[2,3] However, in contrast to well-defined homogeneous catalysts, establishing structure-performance relations and identifying the active sites in heterogeneous systems is challenging due to the inherent material complexity.[3,4] In this regard, employing single-atom heterogeneous catalysts (SACs), containing isolated atoms in discrete chemical environments is an effective approach to enable fundamental and mechanistic studies.[3–7] Beyond this, SACs often exhibit unique performance in diverse reactions due to their high degree of metal dispersion, tunable electronic properties, and unsaturated coordination environments of the active centers in tailored host materials.[7–14] In this regard, the first step in the development of a catalyst design strategy entails a detailed assessment on the impact of metal nuclearity and host effects, from single atoms with defined environments to size-controlled nanoparticles, on reactivity patterns for a given application.[15–17]

A prominent class of reactions, widely used in numerous industrial processes, are hydrogenations,[18–20] which are commonly carried out over supported nanoparticles of precious metals with high sensitivity to their specific ensemble design.[21–27] An example of high practical relevance is the hydrodebromination of dibromomethane (CH_2Br_2) into bromomethane (CH_3Br), an important transformation for the industrial realization of bromine-mediated natural gas upgrading technologies into chemicals and fuels.[28–30] Therein, limited progress has been made toward selective hydrodebromination, where carbon losses in the form of CH_4 and coke represent a major challenge.[30,31] A recent study evaluated the performance of SiO_2-supported nanoparticle-based (NP-based) metal catalysts (1 wt% of Fe, Co, Ni, Cu, Ru, Rh, Ag, Ir, Pt). Therein, at comparable reaction conditions, iron-, cobalt-, copper-, and silver-based catalysts displayed CH_2Br_2 conversion levels of 4–7%, showing consistency with the reported poor hydrodebromination ability of these elements.[30] Among the platinum group metals, selective CH_2Br_2 hydrodebromination to CH_3Br was reported over Ru/SiO_2 (up to 96%, **Table 1**), whereas the CH_3Br selectivity over Rh/SiO_2 (<48%), Ir/SiO_2 (<40%), and Pt/SiO_2 (23%) was

A. J. Saadun, S. K. Kaiser, S. Büchele, Prof. J. Pérez-Ramírez
Department of Chemistry and Applied Biosciences
Institute for Chemical and Bioengineering
ETH Zurich
Vladimir-Prelog-Weg 1, Zürich 8093, Switzerland
E-mail: jpr@chem.ethz.ch

A. Ruiz-Ferrando, S. Pablo-García, E. Fako, Prof. N. López
Institute of Chemical Research of Catalonia (ICIQ)
The Barcelona Institute of Science and Technology
Av. Països Catalans 16, Tarragona 43007, Spain

lower due to coking and over hydrogenation to CH_4, respectively.[31] Despite the promising initial selectivity to CH_3Br, coking and sintering cause the rapid deactivation of Ru-based catalysts. On the contrary, platinum nanoparticles of ≈2 nm show the highest stability all systems investigated. In addition, Pt/SiO_2 displays a turn over frequency (*TOF*) that is *ca.* 8-fold higher than the benchmark ruthenium catalyst (Table 1), which invites further investigations on this metal from an application viewpoint. However, support effects on activity, selectivity, and stability were not explored and no attempts were made to enhance the performance of Pt-based catalysts by nanostructuring of the active site, an approach that has been proven effective for improving catalytic performance in selective dihalomethane hydrodehalogenation.[32] Furthermore, the formulation of structure–performance relationships is hampered by the limited molecular insights available. To date, the binding strength of the metal with CH and Br fragments and the ability to activate H_2 were postulated as activity and selectivity descriptors,[31] leaving ample room for further fundamental investigations.

This encouraged us to systematically study nuclearity and host effects of platinum catalysts in CH_2Br_2 hydrodebromination on their activity, selectivity, and stability. For this purpose, a platform of activated carbon (AC) and nitrogen-doped carbon (NC) supported platinum nanostructures, ranging from single atoms to nanoparticles of gradually increasing size, was adopted. Controlling the functionalization of the carbon host (e.g., N or O, suitable anchoring sites to platinum) and use of thermal activation allowed tuning of the density and structure of the metal coordination sites. By combining catalyst evaluation with in-depth characterization, kinetic analysis, and density functional theory (DFT), we rationalize the activity and selectivity patterns and unravel distinct deactivation mechanisms, thereby providing guidelines for the design of catalysts with improved activity, selectivity, and stability performance.

2. Results and Discussion

2.1. Catalyst Characterization

To study nuclearity and host effects of Pt-catalyzed CH_2Br_2 hydrodebromination, a platform of platinum nanostructures with fixed metal loading (1 wt%) was derived by extending a previously reported synthesis approach,[17] consisting of the dry impregnation of platinum chloride on activated- (AC) and nitrogen doped carbon (NC) carriers, followed by thermal activation and reduction steps. Specifically, thermal activation was performed at different temperatures (T_{act}, 473–1073 K), resulting in catalysts designated as Pt/AC-T_{act} and Pt/NC-T_{act}, which contain platinum ensemble sizes ranging from single atoms with different coordination environment to nanoparticles of 1.3 nm. The Pt/AC-473 and Pt/NC-473 samples underwent the additional reduction step in a H_2-rich atmosphere at elevated temperatures, T_{red}, of 573 and 873 K, with the aim to derive nanoparticles larger than 1.3 nm through enhanced sintering. Those catalysts were denoted as Pt/AC(T_{red}) and Pt/NC(T_{red}) (**Figure 1**a).

Analysis of the porous properties of the as-prepared materials by N_2-sorption (**Table 2**) revealed that the specific surface area and pore volume (S_{BET} = 916–1093 $m^2\ g^{-1}$, V_{pore} = 0.56–0.68 $cm^3\ g^{-1}$) of the AC-supported catalysts are larger than those of the NC-supported catalysts (S_{BET} = 363–545 $m^2\ g^{-1}$, V_{pore} = 0.32–0.42 $cm^3\ g^{-1}$), as expected from the blank supports. Quantification of the metal content by inductively coupled plasma-optical emission spectrometry (ICP-OES) confirmed that the platinum loading of the catalysts were very close to the targeted value of 1 wt% (Table 2). The powder X-ray diffraction (XRD) patterns of Pt/AC-473 and Pt/NC-473 showed broad diffraction peaks compatible with the carbon phase, whereas platinum reflections were not visible (Figure 1b), suggesting the absence of large nanoparticles. In contrast, the Pt/AC(T_{red}) and Pt/NC(T_{red}) samples showed characteristic diffraction patterns of metallic platinum (Figure 1b; Figure S1, Supporting Information), indicating that the additional treatment in H_2 promotes metal sintering. These observations were corroborated with high-angle annular dark-field scanning transmission electron microscopy (HAADF-STEM), highlighting atomically dispersed platinum in the catalysts activated at 473 K, irrespective of the host functionalization (i.e., Pt/NC-473 and Pt/AC-473, Figure 1c). The platinum single atoms remain atomically dispersed at a treatment temperature of 1073 K on NC (Pt/NC-1073), whereas sintering into nanoparticles with an average size of 0.6 and 1.3 nm was observed on AC at 673 and 1073 K (Pt/AC-673 and Pt/AC-1073), respectively (Table 2).[17] The micrographs further revealed the morphological evolution of platinum single atoms to nanoparticles upon thermal treatment in H_2 at 573 and 873 K, progressing to an average size of 2.3 and 3.1 nm in Pt/NC(T_{red}) and 2.9–3.8 nm in Pt/AC(T_{red}) (Figure 1c; Figure S2, Supporting Information). Although nanoparticles are dominant in these materials, the presence of some single atoms cannot be excluded, especially for the catalysts reduced at 573 K. A summary of the catalysts studied herein is presented in Table 2.

The extended X-ray adsorption fine structure (EXAFS) spectra showed no peaks characteristic for the Pt—Pt bonds in the samples treated at 473 K (Figure S3, Supporting Information), which supports the absence of nanoparticles in these samples. Rather, contributions were observed revealing 2.3 ± 0.3 and 3.2 ± 0.3 Cl neighbors in Pt/NC-473 and Pt/AC-473, respectively.[17] The dominating environment of the platinum single atoms in the NC-supported system changes from Cl to N/O-neighbors at a thermal activation temperature of 1073 K. Further analysis by X-ray photoelectron spectroscopy (XPS) was performed to gain a deeper understanding on the chemical state of platinum in the single atoms and nanoparticles

Table 1. Catalysts for CH_2Br_2 hydrodebromination. Data taken from ref. [31].

Catalyst	Reactivity[a]	
	S (CH_3Br [%])	*TOF* [h^{-1}][b]
Ni/SiO_2	64	8
Ru/SiO_2	96	14
Rh/SiO_2	48	32
Pt/SiO_2	23	277

[a]Selectivity to CH_3Br and rate were denoted as *S* and *TOF*, respectively; [b]Average metal particle size in the range of 1.6-2.4 nm. Reaction conditions: CH_2Br_2:H_2:Ar:He = 6:24:4.5:65.5, F_T:W_{cat} = 40 $cm^3\ min^{-1}\ g_{cat}^{-1}$, *T* = 523 K, *P* = 1 bar, and *tos* = 15 min.

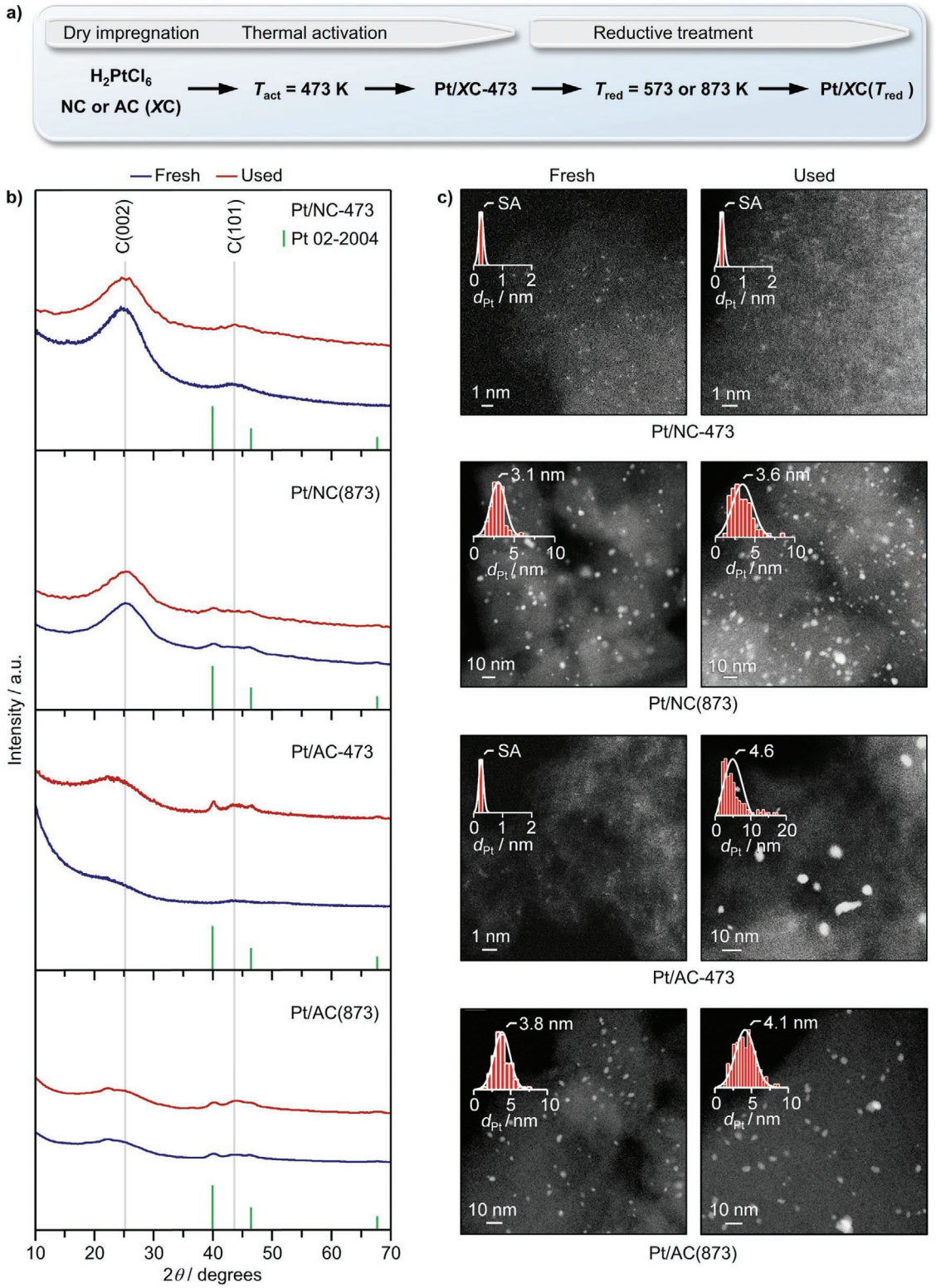

Figure 1. a) Synthetic route for the preparation of carbon-supported platinum nanostructures ranging from single atoms (SA) to nanoparticles. b) XRD patterns and c) HAADF-STEM micrographs with derived particle size distributions of selected catalysts in fresh and used forms. Conditions for used catalysts: CH_2Br_2:H_2:Ar:He = 6:24:5:65, F_T:W_{cat} = 200-500 $cm^3\ min^{-1}\ g_{cat}^{-1}$, T = 523 K, P = 1 bar, and *tos* = 10 h.

(**Figure 2**; Table S1, Supporting Information). The Pt 4f spectra of the single atom-based (SA-based) systems, Pt/AC-473 and Pt/NC-473, showed two main contributions at a binding energy (BE) of 72.4 ± 0.1 and 73.6 ± 0.1eV, which are assigned to Pt(II) and Pt(IV), respectively.[17] This strongly oxidized character of the single atoms in Pt/AC-473 and Pt/NC-473 is

Table 2. Characterization data of the catalysts.

Catalysts	Pt content[a] [wt%]	Fresh (used)[f]			
		S_{BET}[b] [$m^2\ g^{-1}$]	V_{pore}[c] [$cm^3\ g^{-1}$]	d_{Pt}[d] [nm]	Br content[e] [wt%]
Pt/NC-473	0.97	469 (53)	0.38 (0.10)	SA (SA)	0 (5.5)
Pt/NC-1073	0.94	363 (30)	0.32 (0.10)	SA	–
Pt/NC(573)	1.00	488 (232)	0.40 (0.25)	2.3 (3.0)	–
Pt/NC(873)	1.00	545 (215)	0.43 (0.22)	3.1 (3.6)	0 (6.0)
Pt/AC-473	0.94	922 (952)	0.57 (0.59)	SA (4.6)	0 (1.5)
Pt/AC-673	1.02	916 (860)	0.56 (0.54)	0.6	–
Pt/AC-1073	0.97	1093 (1030)	0.68 (0.65)	1.3	–
Pt/AC(573)	1.01	930 (850)	0.58 (0.52)	2.9 (3.7)	–
Pt/AC(873)	0.98	1050 (920)	0.66 (0.56)	3.8 (4.1)	0 (1.1)

[a]ICP-OES; [b]BET model; [c]Volume of N_2 adsorbed at $p/p_0 = 0.98$; [d]Derived from HAADF-STEM micrographs. SA: single atoms; [e]Quantified by XPS; [f]After 10 h in CH_2Br_2 hydrodebromination. Reaction conditions as specified in the caption of Figure 1.

related to the presence of Cl- and N/O-atoms coordinated to platinum (Figures S3 and S4, Supporting Information), in line with the EXAFS analysis. In contrast, chlorine was not detected in the reduced NP-based systems, Pt/AC(873) and Pt/AC(873), and an additional contribution of metallic platinum at a binding energy of 71.2 ± 0.1 eV was observed (Figure 2). However, these systems still show contributions of peaks compatible with Pt(II) and Pt(IV) assignments, likely related to quantum size effects that are most prominent for small nanoparticles.[33] Notably, Pt/NC(873) shows a strong contribution of Pt(II), which is likely related to an increased metal-support interaction of the NC compared to AC.

For the single atoms, a thorough speciation analysis was conducted via simulations by evaluating the stability of platinum in distinct chemical environments, typically co-existing on N-doped carbon (Figure S5, Supporting Information). Among these, the 3N cavity (denoted as "rol3") was found to yield the most stable Pt/NC configuration and was thus selected as the most suitable representative of the active site. Notice that a single atom reference and a platinum bulk reference are employed to assess the thermodynamic limitations of aggregation and the ability of the cavity to adsorb the platinum single atoms.

2.2. Catalyst Evaluation

The gas-phase CH_2Br_2 hydrodebromination was studied at constant reaction temperature (523 K), feed composition (CH_2Br_2:H_2:Ar:He = 6:24:5:65), and pressure (≈1 bar). Comparison of CH_3Br production rates at a space velocity of 200 $cm^3\ min^{-1}\ g^{-1}$ resulted in the following order of decreasing specific activity: Pt/NC(873) > Pt/NC(573) > Pt/NC-1073 >> Pt/AC-1073 > Pt/AC-673 ≈ Pt/AC(873) ≈ Pt/AC(573) ≈ Pt/NC-473 ≈ Pt/SiO_2 (at a space velocity of 40 $cm^3\ min^{-1}\ g^{-1}$) > Pt/AC-473 (**Figure 3**a). Figure 3a displays these trends as a function of the ensemble size, indicating that NP-based systems show a higher activity compared to their SA-based analogues. More detailed, nanoparticles with an average size of 3.1 and 3.8 nm supported on NC and AC, respectively, exhibit ≈1.5-fold higher activity than their SA-based counterparts. With increasing ensemble size, the AC-supported platinum catalysts achieve the maximum activity at a nanoparticle diameter of 1.3 nm, whereas the NC-supported platinum systems seem to reach a maximum at nanoparticle sizes of 2.3 nm. Notably, the reactivity of the benchmark Pt/SiO_2, with an average nanoparticle

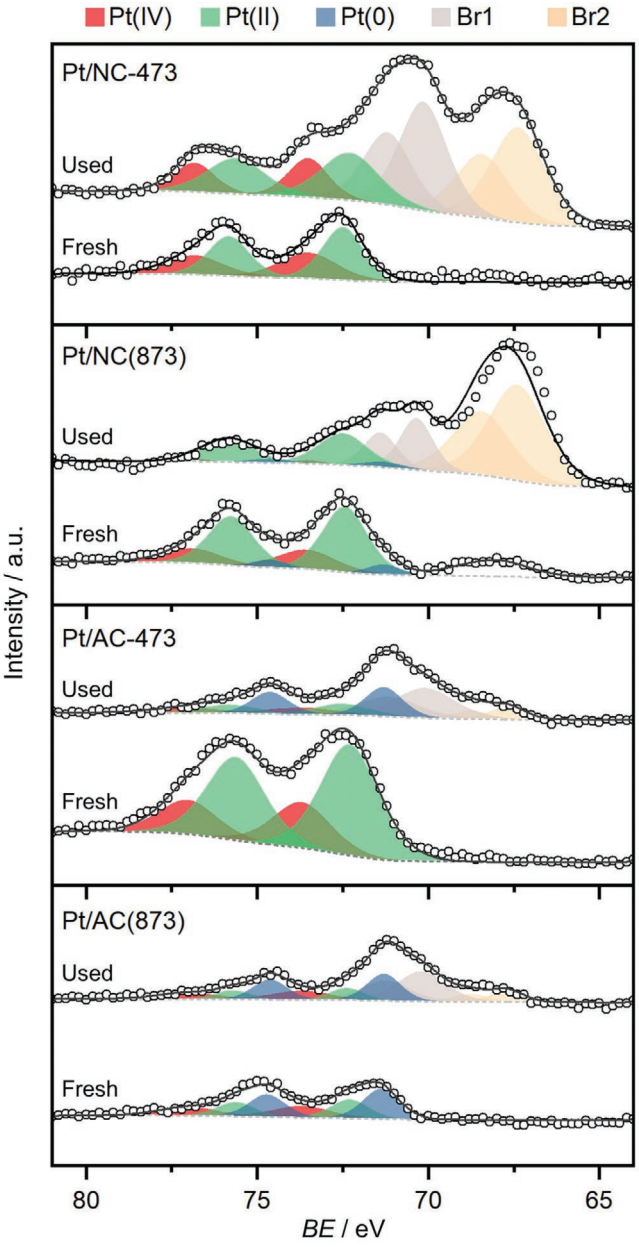

Figure 2. Pt 4f XPS spectra of selected catalysts. The dark gray lines and open circles represent the overall fit and the raw data, respectively, while the colored areas indicate the fit of distinct chemical components. The contribution of the Br 3d signal appearing at a similar binding energy for the used catalysts is separated by fitting two Br species (gray and yellow). Conditions for used catalysts: CH_2Br_2:H_2:Ar:He = 6:24:5:65, F_T:W_{cat} = 200-500 $cm^3\ min^{-1}\ g_{cat}^{-1}$, T = 523 K, P = 1 bar, and *tos* = 10 h.

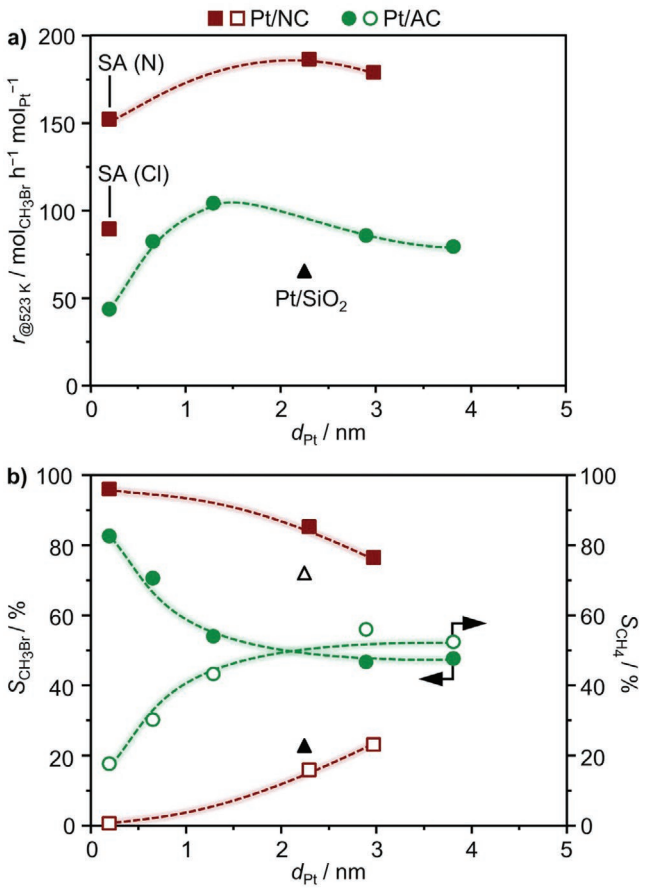

Figure 3. a) Rate of CH_3Br production and b) product selectivity in CH_2Br_2 hydrodebromination over the catalysts as a function of the average platinum particle size (d_{Pt}). In panel (a) the activity was assessed at a constant space velocity of F_T:W_{cat} = 200 cm^3 min^{-1} g_{cat}^{-1}, while product selectivities in (b) were determined at ≈20% CH_2Br_2 conversion achieved by adjusting the space velocity in the range of F_T:W_{cat} = 200-500 cm^3 min^{-1} g_{cat}^{-1}. Other reaction conditions: CH_2Br_2:H_2:Ar:He = 6:24:5:65, T = 523 K, P = 1 bar, and *tos* = 15 min. The triangle indicates the performance of Pt/SiO_2, whereas SA stands for single atoms.

size of 2.2 nm, were threefold lower than the NC-supported platinum nanoparticles with comparable sizes. Furthermore, NC-supported single atoms with an N/O-coordination environment displayed ≈1.5-fold higher activity compared to their Cl-coordinated analogues. The higher activity achieved with the N/O-coordination can be explained by the catalytic role of the matrix on the reaction, where, as proposed in the literature and as shown in density functional theory simulations (vide infra), the N-sites can store hydrogen atoms, leaving the metal center free for coordination.[7]

The product distribution over the catalysts was compared at ≈20% CH_2Br_2 conversion, achieved by adjusting the space velocity (Figure 3b). Remarkably, single atoms supported on NC demonstrate unparalleled selectivity to CH_3Br (up to 98%) and low propensity to CH_4 (<20%), regardless of the host coordination environment, whereas platinum single atoms on AC exhibited a CH_3Br selectivity of ≈84%. These results indicate that SA-based platinum catalysts are able to suppress over hydrogenation pathways, which is a major challenge in this reaction. The gradual increase of selectivity to CH_4 at the expense of CH_3Br formation with increasing platinum ensemble size, from single atoms to nanoparticles of ≈4 nm, confirms the superior selectivity performance of single atoms compared to their nanoparticle counterparts (Figure 3b). The CH_3Br selectivity attained over the NC-supported single atoms rivals that of SiO_2-supported ruthenium nanoparticles (up to 96%), the most selective hydrodebromination catalyst reported so far.[31] Moreover, the selectivity performance over the carbon-supported platinum catalysts is dependent on the type of host, whereby NC-supported systems exhibit higher CH_3Br selectivity than their AC-supported counterparts, suggesting that N-functionalities play a central role in the reaction (vide infra).

The established activity and selectivity patterns were complemented with stability tests to gain a complete picture of the performance of each catalytic system (**Figure 4**). These tests were performed at an initial conversion level of ≈20% (Figure S6, Supporting Information). Upon exposure to the reaction environment for 10 h, the SA-based catalysts displayed activity losses up to 70% (compared to the initial performance). The NC-supported platinum single atoms show a significant CH_2Br_2 conversion loss in the first 2 h on stream (≈60%, Figure 4a), whereas a gradual, though substantial depletion of activity (70% drop) was observed over the AC-supported single atom system (Figure 4b). On the other hand, NP-based materials preserved their initial activity better, displaying activity losses in the range of 10–38%. To allow a direct comparison of the stability performance, the deactivation was expressed with the constant k_D (Figure 4c), which indicates the activity losses per hour, and which was derived via linear regression of the data in the time-on-stream (*tos*) range that is indicated in Figure S6, Supporting Information. Displaying the k_D values as a function of the platinum ensemble size emphasized the observed patterns and highlighting host- and platinum ensemble size roles on stability (Figure 4c). Depletion of activity was appended by moderate changes in the product distribution over the catalysts. With *tos*, the NC-supported SA-based Pt/NC-473 and Pt/NC-1073 maintained their high performance with >98% selectivity to CH_3Br, suggesting preservation of the single atom nanostructure. On the other hand, activity losses were accompanied by an increase of CH_4 selectivity (from 18% to 33%, at the expense of CH_3Br) over SA-based Pt/AC-473, likely due to sintering of the active phase (vide infra). NP-based catalysts generally showed no pronounced selectivity changes with *tos*.

2.3. Deactivation Mechanisms

To examine the development of the materials during exposure to the reaction environment, detailed characterization of selected used catalysts by N_2-sorption, XRD, HAADF-STEM, and XPS was performed, revealing three main deactivation mechanisms: i) fouling by coking, ii) active phase sintering, and iii) bromination. N_2-sorption indicated the significant decrease in the specific surface area and pore volume (S_{BET} = 215–30 m^2 g^{-1}, V_{pore} = 0.25–0.10 cm^3 g^{-1}) of the NC-supported systems (Table 2), highlighting the poor stability of the carrier. The decrease of S_{BET} and V_{pore} was more pronounced over the NC-supported SA-based catalysts than their NP-based equivalents, suggesting that the former were more affected by fouling. In contrast,

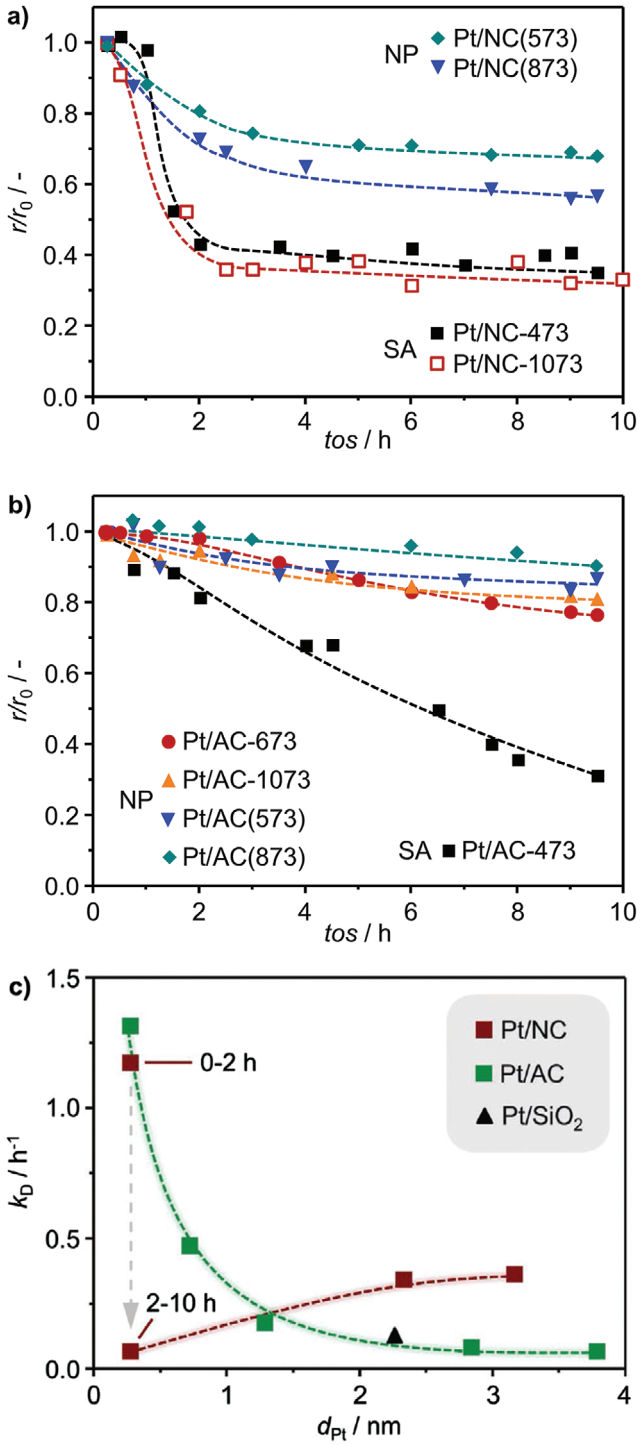

Figure 4. Relative rate of CH_2Br_2 hydrodebromination as a function of time on stream over the a) NC-supported and b) AC-supported platinum catalysts. c) The deactivation constants (k_D) as a function of the average platinum particle size (d_{Pt}). The triangle in (c) indicates the performance of Pt/SiO_2. Reaction conditions: CH_2Br_2:H_2:Ar:He = 6:24:5:65, F_T:W_{cat} = 200-500 $cm^3\ min^{-1}\ g_{cat}^{-1}$, T = 523 K, and P = 1 bar. SA and NP stand for single atoms and nanoparticles, respectively.

AC-supported catalysts showed minimal changes in S_{BET} and V_{pore}, likely due to the absence of coking mechanisms. Furthermore, the XRD profiles of Pt/NC-473, Pt/NC(873), and Pt/AC(873) resemble those of the fresh materials (Figure 1b), implying that no severe active phase sintering occurred over these materials. On the other hand, a strong reflection assigned to metallic platinum was detected for used Pt/AC-473, indicating that active phase restructuring occurred, which was confirmed by HAADF–STEM microscopy showing the increase of the average platinum ensemble size from single atoms to nanoparticles of 4.6 nm (Figure 1c). The micrographs further disclosed the absence of nanoparticles on used Pt/NC-473, whereas modest platinum sintering was distinguished over the used NP-based systems, Pt/NC(T_{red}), and Pt/AC(T_{red}) (Table 2). Interestingly, the SA-based Pt/AC-473 displays the highest deactivation rate despite sintering of its active phase into nanoparticles, which were found to be more reactive than single atoms (Figure 3a). Therefore, the observed activity losses likely originate, beside bromination, from the distinct surface sites, which alter the coverage of the surface species and gives rise to a different reactivity compared to other nanoparticles with a similar size. As is recognized in other hydrogenation studies,[24,34] the surface concentration of active corners and edges could significantly alter the hydrogenation performance. This possible influence of the site type in nanoparticles on reactivity broadens the mechanistic diversity of hydrodebromination reactions over platinum surfaces, and deserves to be tackled in future dedicated studies.

XPS analysis was conducted to investigate the chemical state of platinum and the role of surface bromination. The similar binding energies of the Pt 4f and Br 3d signals require a simultaneous fitting approach of distinct chemical components for both elements (Figure 2; Table S1, Supporting Information). The spectra revealed prominent surface bromination for NC-based materials (up to 6 wt% Br), whereas their AC-based counterparts were less affected by Br-poisoning (up to 1.5 wt% Br) (Table 2; Figure S4, Supporting Information). The total Br-content in the catalysts was mainly determined by the carrier functionalization, since NP-based systems displayed comparable Br-content to their SA-based counterparts. For the SA-based materials, no significant change in the chemical state is observed in fresh and used Pt/NC-473, with similar contributions from Pt(II) and Pt(IV), and no peak designated to metallic platinum in Pt/NC-473 (Figure 2), which is well in line with the suggested absence of platinum sintering. In contrast, Pt/AC-473 is reduced with a clear peak of Pt(0) appearing in the used catalyst, showing a comparable chemical state as its NP-based analogue, Pt/NC(873). On the other hand, the NP-based systems display a contribution of Pt(II) (Figure 2), which was less pronounced in the used Pt/AC(873) catalyst, likely due to the bromination of the active phase.

In view of a potential industrial application, the possibility to regenerate Pt/NC-473 was investigated. Whereas the premier cause of activity losses with *tos* is coking, an attempt was made to restore the initial activity (21% CH_2Br_2 conversion) by removal of the carbonaceous residues from the used catalyst, which exhibited a CH_2Br_2 conversion of 7% after 10 h on-stream, via thermal treatment in 20 vol% O_2 in He (F_T = 20 cm^3 STP min^{-1}). Since N-doped carbon remains stable up to 573 K under these conditions,[17] the treatment was conducted at slightly lower temperatures (523 K) for 6 h. The treated catalyst displayed marginal regeneration of its hydrodebromination activity with a CH_2Br_2 conversion level of 11% after 15 min on-stream, suggesting that the structural

changes of the support are not reversible. Moreover, the selectivity to CH_3Br is high (86%), though still lower than the initial performance (98%), possibly due to restructuring of the active phase. The changes introduced in the host and the active sites upon catalyst treatment is beyond the scope of this study and deserves attention in future dedicated studies. These results highlight the fact that catalyst robustness in CH_2Br_2 hydrodebromination remains a major challenge.

2.4. Mechanistic and Kinetic Studies

In nanoparticles, a fraction of the atoms, located in the bulk, are not exposed to the reactants, whereas each of the atomically dispersed single atoms could react with CH_2Br_2 and H_2. Moreover, in contrast to platinum nanoparticles, the single atoms do not have a neighboring platinum atom, which could affect their interaction with the reactant molecules. Expressing the catalytic activity per surface platinum atom will provide first insights on these effects. To this end, the turnover frequency (*TOF*) of selected SA-based systems was compared (at a similar space velocity of 200 $cm^3\ min^{-1}\ g_{cat}^{-1}$) with their NP-based counterparts (**Figure 5**). The dispersion of platinum in the nanoparticle-based catalysts was assessed by CO chemisorption. The activity of the catalysts decreased in the following order: Pt/AC(873) ≈ Pt/NC(873) >> Pt/NC-473 > Pt/AC-473, with dispersion values of 31% and 26% in Pt/NC(873) and Pt/AC(873), respectively. The NP-based systems exhibit a higher *TOF* compared to their SA-based analogues (>6 times), suggesting that neighboring Pt-atoms participate in the reaction, thereby enhancing the activity. The effects of the neighboring atoms on activity is further investigated with density functional theory simulations (vide infra). Furthermore, in line with previous observations (Figure 3a), AC-supported single atoms display lower reactivity than their NC-supported counterparts. In comparison with the benchmark Pt/SiO_2, carbon-supported platinum nanoparticles with a comparable size (≈2 nm) achieve a considerably higher *TOF* (≈3 times), while the *TOF* of the carbon-supported SA-based catalysts are of the same order of magnitude as those observed over Pt/SiO_2 with an average nanoparticle size of 2.2 nm.[31] These results emphasize the impact of the carbon carrier on the catalytic activity of the metal, improving the utilization of the platinum atoms in carbon-supported systems compared to those supported on inert SiO_2, which has minimal interaction with the active phase.

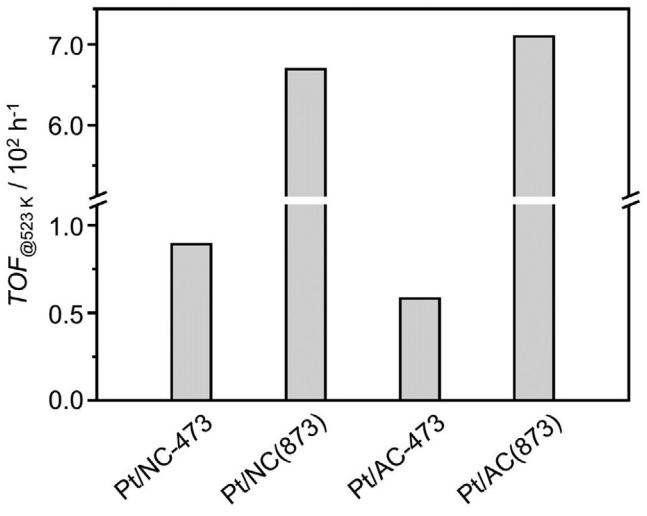

Figure 5. Turnover frequencies over selected catalysts. Each catalytic data point was gathered using materials in fresh form to exclude the possible influence of catalyst deactivation. Reaction conditions: CH_2Br_2:H_2:Ar:He = 6:24:5:65, F_T:W_{cat} = 200 $cm^3\ min^{-1}\ g_{cat}^{-1}$, T = 523 K, P = 1 bar, and *tos* = 15 min.

To obtain a molecular-level understanding of the different activity and selectivity patterns, density functional theory (DFT) simulations were performed. The reaction network with the pathways leading to CH_3Br, CH_4, and C (coke) is described (**Figure 6**) and the associated thermodynamic and kinetic parameters were calculated (Table S2, Supporting Information) for the most stable Pt species in the three materials. The Gibbs energies for the reaction profiles over the NC- and AC-supported platinum single atoms and the comparative Pt(111) surface representing the nanoparticles are shown in **Figure 7**. The temperature and pressures in the Gibbs terms were those from experiments. Unfortunately, the direct use of the span model[35] or direct comparison to the *TOF* is not possible due to several reasons including: i) the diversity of potentially active sites in the N-doped material (herein only one of the configurations is presented for conciseness); and ii) the selectivity issue, particularly with the formation of coke, that is difficult to be addressed through the two-state span model.

The network starts by the dissociative adsorption of CH_2Br_2 on the Pt(111) surface, leading to CH_2Br*. However, this intermediate is labile and the second Br is easier to lose than the first one. This occurs because breaking the second C—Br bond is compensated by the formation of a bridge species with two platinum atoms, Pt-CH_2-Pt, thereby fulfilling the valence of the C atom via an ensemble considering the involvement of several metal atoms (CH_2Br sits on top; thus only one atom forms the ensemble). Such cascade decomposition effects have been described in literature and are a direct consequence of the continuous nature of the metal surface and linear-scaling contributions. Typically, they lead to the intermediate that optimally fills the best coordination sites (CH*).[36] Therefore, the main gaseous product for the platinum nanoparticle is the recombination with the hydrogen atoms on the surface to generate CH_4.

In N-doped carbon, several potential coordination sites for platinum atoms co-exist (Figure S5, Supporting Information). While the most widely studied fourfold coordinative pockets cannot trap platinum in an active form, the 3N cavity (denoted as "rol3") is optimally suited to yield an active platinum ensemble which may accommodate intermediates with only one valence left, that is, CH_3 or alike, but is not prone to generate CH_2 species. The formation of the methylene (CH_2*) fragment implies the formation of a double bond with the platinum atom that, due to the geometric constraints of the hybridization, fulfills the valence in a less effective way than an increased number of metal atoms in an ensemble with a continuum platinum surface. This agrees with our results; CH_2Br_2 adsorbs on different platinum sites in the NC- and AC-carrier (Figure 7). The adsorption is quite exothermic in all cases and leads to H_2BrC-Pt-Br fragments. From this intermediate, the following

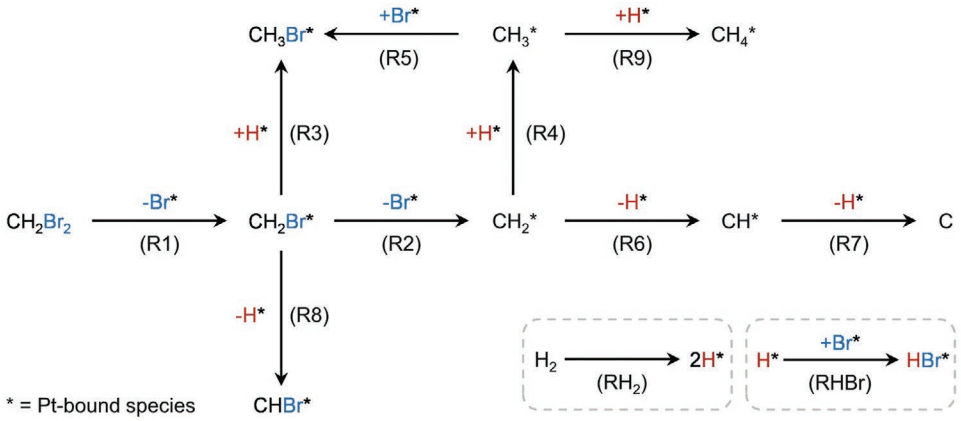

Figure 6. Reaction network of CH_2Br_2 hydrodebromination showing the pathways leading to CH_3Br, CH_4, and C (coke) formation. Dashed boxes show elementary steps for the formation of HBr and the activation of H_2. The labels in parentheses indicate thermodynamic and kinetic parameters that are detailed in Table S2, Supporting Information.

decompositions can in principle happen: i) Br elimination of the scaffold to H_2C-Pt-Br; ii) Br_2 elimination with concomitant formation of H_2C-Pt; or iii) H elimination leading to HBrC-Pt-Br. Out of these structures, reactions (i) and (ii) are very high in energy due to the difficulties of platinum atom to accommodate the methylene group via the ensemble and also since the platinum in the scaffold is already electron rich due to the interaction with the nitrogen atoms in the host. Only path (iii) is reachable, leading to the CHBr intermediate that is less electronically compromised (due to the electron acceptor nature of Br). The Pt-CHBr species is very reactive and can be the origin of the instability found for the NC-supported single atom catalysts. The H_2BrC-Pt-Br system can also dissociatively adsorb H_2, with one H atom ending in the platinum site and the other left in the basic sites of the host. This would be promoted by the basicity of the cavity, in line with the enhanced reactivity observed over NC-supported platinum catalysts compared to the AC-supported analogues. The dissociation is relatively easy, followed by the facile formation of HBr and CH_3Br on the single atom, thereby re-establishing the active site. The full reaction mechanism including all activation steps can be facilitated by the single atom site in both the NC- and AC-supported systems, which includes its immediate coordination environment (N- or O-moieties). Therefore, participation of the host in SA-based catalysts is crucial to enable the adsorption of CH_2Br_2 and H_2 since it traps H atoms that can be later transferred to other moieties. On the models with AC as host (the anchoring points are oxygen defects as shown in Figure S5, Supporting Information), the H_2BrC-Pt-Br dissociation occurs easily, leading to square planar structures which are prone to decomposition and release of HBr. The remaining moieties would trigger polymerization reactions that would lead to undesired products. On the other hand, if H_2 is activated it leads to the weakening of the Pt—AC bond, which likely leads to unstable single atoms, making them mobile and thus resulting in the potential formation of nanoparticles by diffusion and coalescence.

Further insights were gained by conducting kinetic analysis over the selected systems, showing differences in the apparent activation energies with values of 39 (Pt/AC-473), 37 (Pt/NC-473), 27 (Pt/NC(873)), and 24 kJ mol^{-1} (Pt/AC(873)) (**Figure 8**a). The values for the NP-based systems, ≈24 and 27 kJ mol^{-1}, are lower than those attained over platinum nanoparticles supported on SiO_2 (34 kJ mol^{-1}).[31] Rather, these apparent activation energies are in the same range as the values obtained over SA-based catalysts (37 and 39 kJ mol^{-1}), in line with the comparable *TOF* over these materials. From the reaction profiles, the energies required for the most energetic steps are taken as representative for the apparent activation energies. The calculations confirm that the nanoparticles have a slightly lower apparent activation energy than the SA-based systems (≈15 kJ mol^{-1}, CH_2Br_2 dissociation step), while the configuration employed to represent the Pt/NC-473 system shows a larger value (59 kJ mol^{-1}, HBr elimination). The deviations are due to the lack of support and coverage effects on the platinum nanoparticle models and the use of a single configuration to represent the material. The rapid deactivation of the AC-supported SA-based catalyst prevents us from using the computed reaction profiles as side paths dominate the apparent activation energy.

Furthermore, upon increasing the partial H_2 pressure from 12 to 72 kPa, the normalized reaction rate increases significantly over the NP-based catalysts (up to ≈6 times), whereas the SA-based systems were less affected (up to 2.5 times) by these changes in feed composition (Figure 8b). In addition, the increase of partial H_2 pressure showed no influence on the product distribution of SA-based systems, confirming their low sensitivity to increasing inlet H_2 concentrations. The derived partial orders in H_2 are higher over NP-based catalysts, with values of 1.00 and 0.83 for Pt/AC(873) and Pt/NC(873), respectively, while the SA-based systems display partial orders of 0.60 (Pt/AC-473) and 0.41 (Pt/NC-473). The selectivity to CH_3Br attained over these systems correlates inversely with the partial orders in H_2, being higher for lower partial orders in H_2. This agrees with the reaction profiles and the computed main paths obtained by DFT.

The lower reaction order in H_2 of SA-based catalysts and their higher apparent activation energy, compared to their NP-based counterparts, can be rationalized by their ability to activate H_2 and store H-atoms that can react with surface species. The geometry of nanoparticles enables facile H_2 dissociation

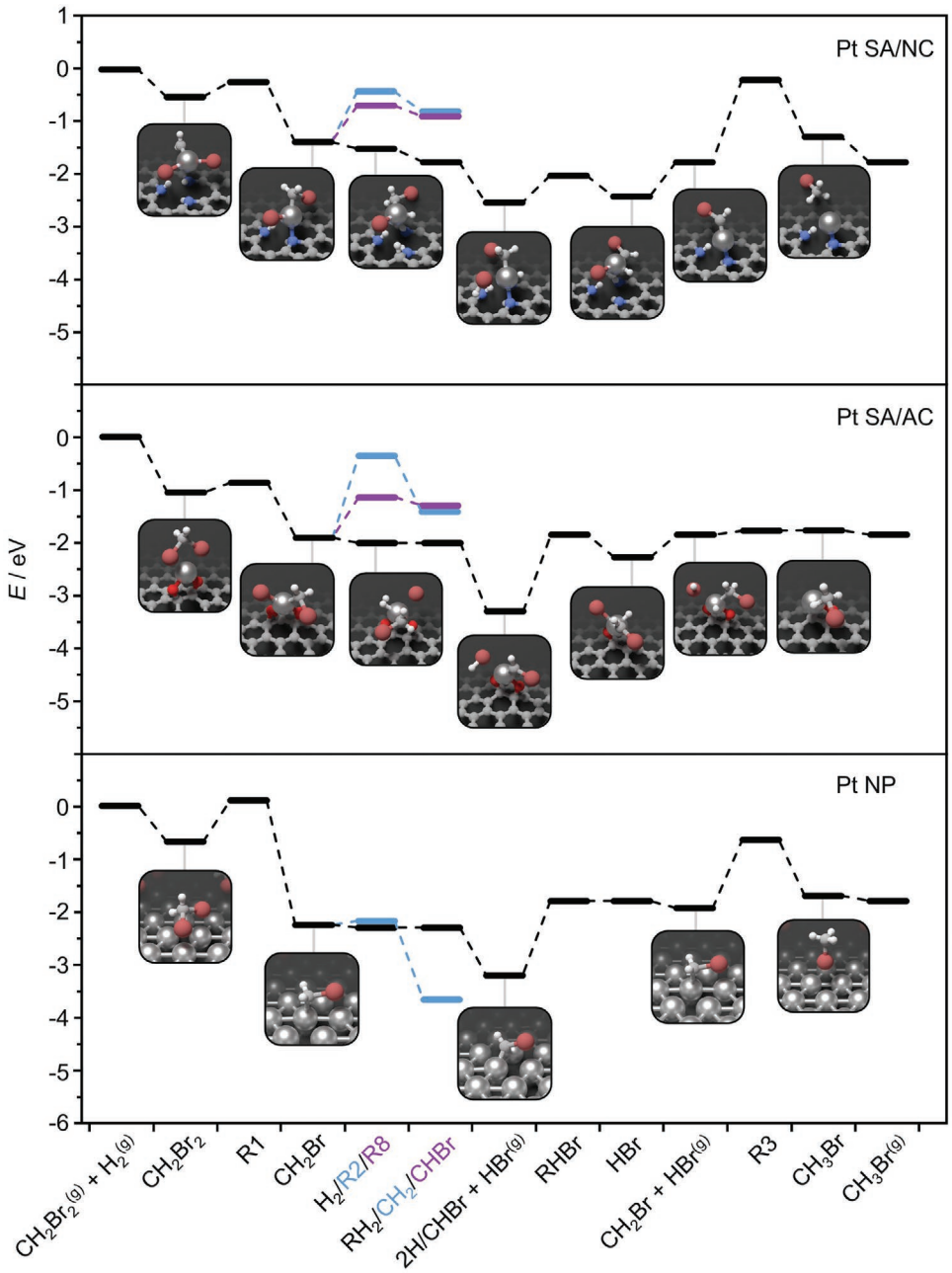

Figure 7. Gibbs energy profiles and schematic depictions of CH_2Br_2 hydrodebromination over platinum single atoms (SA) and a platinum(111) surface representing the nanoparticles (NP). Color code: C, gray; N, blue; O, red; H, white; Pt, metallic gray; Br, brown. The temperatures and pressures are those of the experiments: CH_2Br_2:H_2:Ar:He = 6:24:5:65, T = 523 K, and P = 1 bar.

(via the homolytic process) and allows higher hydrogen coverage, which is limited on single atoms. As for the single atoms in the carbon, the cavities are crucial and the presence of N-functionalities improves ability to heterolytically split H_2 into H-atoms for the SA-based systems.[7] H_2 activation is crucial and explains the higher reactivity of Pt/NC-473 compared to Pt/AC-473. In addition, the production of CH_3Br requires a single H-atom, therefore the partial order in H_2 of selective SA-based systems is ≈0.5, indicating that the reaction of the second H-atom is rate limiting. In contrast, the partial order in H_2 of NP-based systems is *ca.* 1.0, matching their higher propensity to generate CH_4. Moreover, NC-supported systems display lower partial orders in H_2 and higher CH_3Br selectivity than their AC-supported counterparts. This is likely due to the higher halogen uptake on NC-supported systems, a factor which was found to be key in steering the reaction pathway in selective dihalomethane hydrodehalogenations.[32] These kinetic fingerprints suggest that the reaction occurs with different mechanisms over platinum single atoms compared to nanoparticles, and corroborate the crucial role of the host in order to potentially alter the adsorption and/or desorption of the different species.

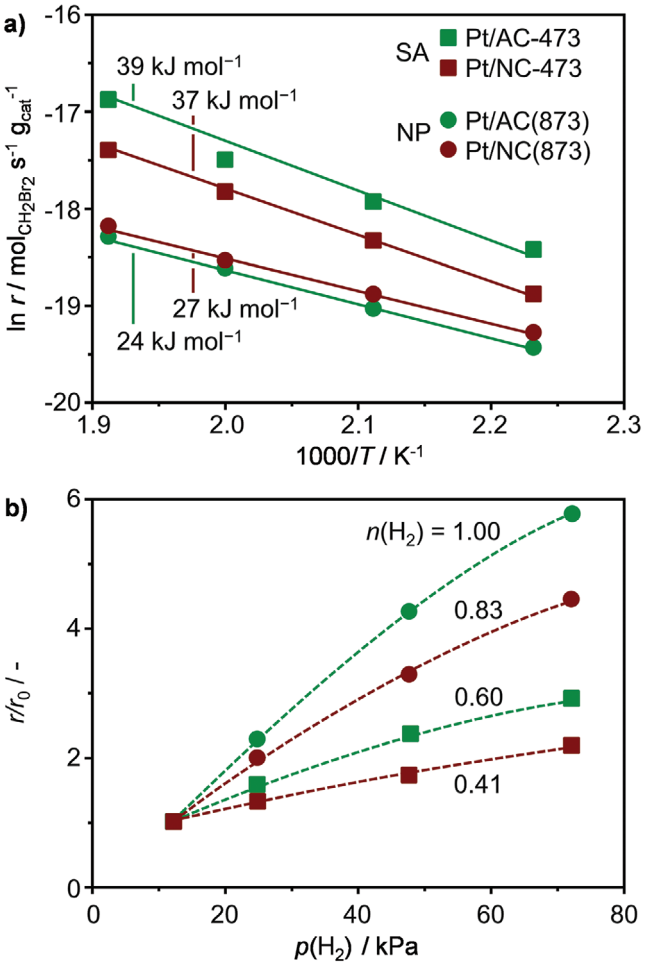

Figure 8. Rate of CH_2Br_2 hydrodebromination of selected catalysts as a function of a) temperature and b) inlet partial pressure of H_2. Each catalytic data point was gathered using materials in fresh form to exclude the possible influence of catalyst deactivation. Reaction conditions: a) CH_2Br_2:H_2:Ar:He = 6:24:5:65, F_T:W_{cat} = 100–500 cm^3 min^{-1} g$_{cat}^{-1}$, T = 448-523 K; b) CH_2Br_2:H_2:Ar:He = 6:6–72:5:17–83, F_T:W_{cat} = 200–800 cm^3 min^{-1} g$_{cat}^{-1}$, T = 523 K. All tests were conducted at P = 1 bar and *tos* = 15 min. SA and NP stand for single atoms and nanoparticles, respectively.

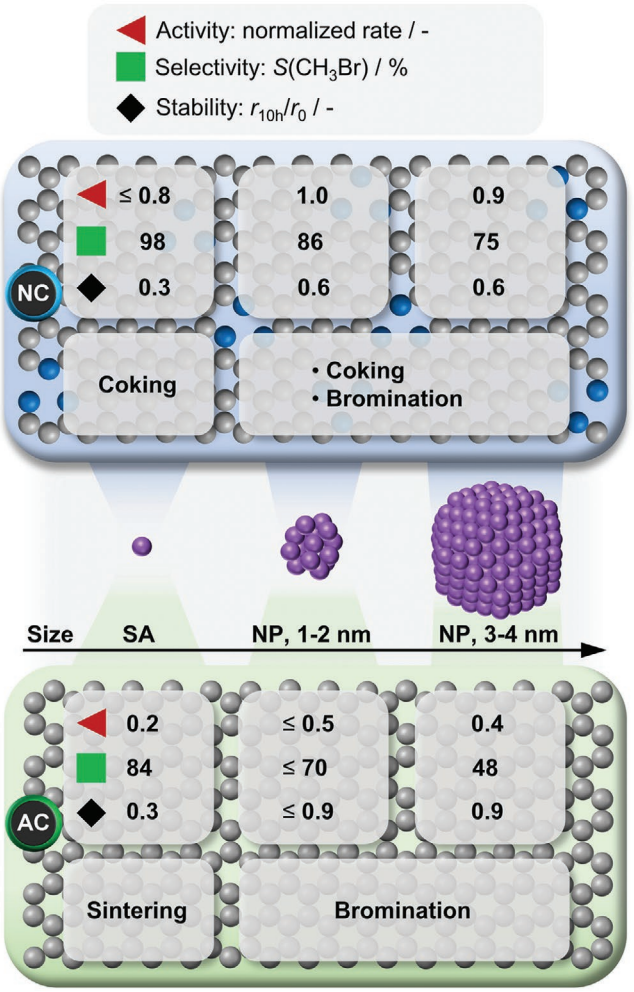

Figure 9. Summary scheme of nuclearity and host effects on the reactivity of carbon-supported platinum catalysts for CH_2Br_2 hydrodebromination, with indication of the main modes of deactivation. SA and NP stand for single atom and nanoparticle, respectively. The conditions specified in the captions of Figures 3 and 4 apply here.

3. Conclusions

In conclusion, a platform of NC- and AC-supported platinum nanostructures, ranging from single atoms to nanoparticles of ≈4 nm was derived to systematically assess nuclearity and host effects on the catalyst activity, selectivity, and stability performance in CH_2Br_2 hydrodebromination, through coupling in-depth characterization, kinetic analysis, and density functional theory (DFT). Catalytic evaluation revealed that i) SA-based catalysts exhibit unparalleled CH_3Br selectivity of up to 98%, whereas the formation of CH_4 (selectivity < 60%) is increasingly favored over larger nanoparticles, ii) the specific activity reaches a maximum over platinum nanoparticles with an average size in the range of 1.3–2.3 nm, thereby achieving up to a threefold higher CH_3Br production rate and *TOF* than Pt/SiO_2, and iii) NC-supported platinum catalysts are more active and selective to CH_3Br compared to their AC-supported analogues. Moreover, NP-based systems displayed improved stability compared to their SA-based analogues, where the functionalization of the carbon host determined the mode of deactivation. Specifically, on AC, sintering of the single atoms was the major deactivation path, while on NC, the single atoms remained structurally stable, but coking prevailed due to the generation of unstable intermediate species during the reaction. A summary scheme of the carbon host and platinum nuclearity effects on catalyst activity, selectivity, and stability in CH_2Br_2 hydrodebromination with the main modes of deactivation is presented in **Figure 9**.

Kinetic and mechanistic studies emphasized the role of N-functionalities in the host, which can store H-atoms thereby enhancing activity. NC-supported materials displayed higher bromine uptake than their AC-supported counterparts, which likely suppressed over-hydrogenation pathways as corroborated by the lower reaction orders with respect to H_2. Furthermore, in contrast to single atoms, the facile dissociation of H_2 and, due to the geometry, higher availability of surface H-atoms

over nanoparticles promotes CH_4 generation. The findings presented in this study highlight the potential of nanostructuring in CH_2Br_2 semi-hydrogenation, opening up options for the development of improved catalytic systems.

4. Experimental Section

Catalyst Preparation: Carbon-supported Pt-catalysts with Pt-nanostructures varying from single atoms to nanoparticles were prepared following the protocols reported by Kaiser et al.[17] Nitrogen-doped carbon (NC) and commercially available activated carbon (AC, Norit ROX 0.8) were ground and sieved into particles of 0.4–0.6 mm prior to their use as supports. The platinum precursor, chloroplatinic acid (H_2PtCl_6, ABCR, 99.9%, 40.0 wt% Pt), was dispersed on the supports via incipient wetness impregnation. Appropriate amounts of the metal precursor required to obtain a platinum content of 1 wt% in the final catalyst were dissolved in deionized water (1.5 $cm^3\ g^{-1}$) and added dropwise to the carbon carriers under continuous magnetic stirring for 2 h. The impregnated solids were dried at 473 K for 16 h in static air (heating rate 5 K min^{-1}) followed by a thermal activation step at higher temperatures, as indicated in the respective sample code (T_{act} = 473–1073 K), yielding two series of Pt catalysts, Pt/NC-T_{act}, and Pt/AC-T_{act}. The Pt/NC-473 and Pt/AC-473 catalysts underwent an additional thermal reductive treatment in 20 vol% H_2/He (PanGas, purity 5.0) flow for 3 h at elevated temperatures (T_{red} = 573 or 873 K, heating rate 10 K min^{-1}) and were denoted as Pt/NC(T_{red}) and Pt/AC(T_{red}). The synthesis steps of the catalysts developed in this study with their respective sample codes is given in Figure 1a.

Catalyst Characterization: Powder X-ray diffraction (XRD) was measured using a PANalytical X'Pert PRO-MPD diffractometer with Cu-*Kα* radiation (λ = 1.54060 Å). The data was recorded in the 10°–70° 2θ range with an angular step size of 0.017° and a counting time of 0.26 s per step. N_2 sorption at 77 K was measured in a Micromeritics TriStar II analyzer. Samples (≈0.1 g) were evacuated to 50 mbar at 573 K for 12 h prior to the measurement. The Brunauer–Emmett–Teller (BET) method was applied to calculate the total surface area, S_{BET}. The pore volume, V_{pore}, was determined from the amount of N_2 adsorbed at a relative pressure of p / p_0 = 0.98. The platinum content in the catalysts was determined by inductively coupled plasma-optical emission spectrometry (ICP-OES) using a Horiba Ultra 2 instrument equipped with photomultiplier tube detection. The solids were dissolved in a HNO_3:H_2O_2 = 3:1 mixture under sonication until the absence of visible solids. CO pulse chemisorption was performed on a Thermo TPDRO 1100 set-up equipped with a thermal conductivity detector. Prior to the analyses, the NP-based samples (≈0.2 g) were pretreated at 423 K under flowing He (20 cm^3 STP min^{-1}) for 30 min, and reduced at 523 K under flowing 5 vol% H_2/He (20 cm^3 STP min^{-1}) for 30 min. Thereafter, 0.344 cm^3 of 1 vol% CO/He were pulsed over the catalyst bed every 4 min at 308 K. To avoid desorption of CO, the interval between successive pulses was minimized. The platinum dispersion was calculated using an atomic surface density of 1.47 × 10^{19} atoms m^{-2} and an adsorption stoichiometry of Pt/CO = 1. Scanning transmission electron micrographs with a high-angle annular dark-field detector (HAADF–STEM) were acquired on a HD2700CS (Hitachi) microscope operated at 200 kV. All samples were dispersed in ethanol and some droplets were deposited onto lacey carbon coated copper grids and dried in air. The size distribution of the platinum nanostructures was obtained by examining more than 100 particles. X-ray photoelectron spectra (XPS) were acquired on a Physical Electronics Quantum 2000 instrument using monochromatic Al-*Ka* radiation, generated from an electron beam operated at 15 kV, and equipped with a hemispherical capacitor electron-energy analyzer. The samples were analyzed at constant analyzer pass energy of 46.95 eV. The spectrometer was calibrated for the Au $4f_{7/2}$ signal at 84.0 ± 0.1 eV. The envelopes were fitted by mixed Gaussian–Lorentzian component profiles after Shirley background subtraction. The different platinum species were fitted as previously reported (i.e., peak positions fixed ±0.1 eV, full width at half maximum (FWHM) constrained, spin orbit coupling 3.33 eV).[17] A contribution for Pt(0) was only implemented for samples where nanoparticles were detected by HAADF-STEM. The contribution of the Br $3d^{5/2}$ signal in brominated used catalysts was fitted with two chemical states at 70.1±0.2 eV (Br1, attributed to Br—C)[37] and 67.4±0.2 eV (Br_2, attributed to adsorbed Br_2 or Br—Pt).[38,39] The Br 3d(3/2) peaks originating from spin orbit coupling were fixed at a distance of 1.05 eV and constrained to the same FWHM as the corresponding 3d(5/2) peaks. The bromine content was quantified based on the measured C 1s, N 1s, O 1s, Br 3p and the fitted Pt 4f signals using relative sensitivity factors (provided by PHI-MultiPak software), which were corrected for the system transmission function. X-ray absorption fine structure (XAFS) measurements at the Pt L_2 and L_3-edge were carried out at the SuperXAS beamline of the Swiss Light Source. The incident photon beam provided by a 2.9 T superbend magnet was selected by a Si(111) channel-cut Quick-EXAFS monochromator. The rejection of higher harmonics and focusing were achieved with rhodium-coated collimating and toroidal mirrors, respectively, at 2.5 mrad. The beamline was calibrated using Pt foil. The area of sample illuminated by the X-ray beam was 0.5 mm × 0.2 mm. The catalysts (≈0.3 g) were finely ground, mixed homogeneously with five parts of cellulose, and pressed into 13 mm diameter pellets. All spectra were recorded in transmission mode at room temperature. The X-ray absorption near-edge structure (XANES) spectra were calibrated by measuring Pt foil simultaneously with each sample. The extended X-ray absorption fine structure (EXAFS) spectra were acquired with a 1 Hz frequency (0.5 s per spectrum) and then averaged over 10 min. The procedures for analysis and fitting of the EXAFS spectra are reported elsewhere.[17]

Catalyst Evaluation: The hydrodebromination of CH_2Br_2 was carried out at ambient pressure in a continuous-flow fixed-bed reactor set up. H_2 (PanGas, purity 5.0), He (carrier gas, PanGas, purity 5.0), Ar (internal standard, PanGas, purity 5.0) were dosed by a set of digital mass flow controllers (Bronkhorst) and liquid CH_2Br_2 (Acros Organics, 99%) was supplied by a syringe pump (Fusion 100, Chemyx) to a vaporizer unit operated at 393 K. A quartz reactor (internal diameter, d_i = 12 mm) was loaded with the catalyst (catalyst weight, W_{cat} = 0.1–0.25 g, particle size, d_p = 0.4–0.6 mm) and heated to the desired temperature (T = 448–523 K) in an electrical oven under He flow. The catalyst bed was allowed to stabilize for at least 10 min at desired temperature before the reaction mixture was fed at total volumetric flow (F_T) of 20 cm^3 STP min^{-1} and desired feed composition of CH_2Br_2:H_2:Ar:He = 6:24:5:65 (vol%). A composition of CH_2Br_2:H_2:Ar:He = 6:6-72:5:17-83 was applied for the kinetic tests. Downstream linings were heated at 393 K to prevent the condensation of unconverted reactants and/or products. The content of carbon-containing compounds (CH_2Br_2, CH_3Br, and CH_4) and of Ar in the reactor-outlet gas stream was quantified online via a gas chromatograph equipped with a GS-Carbon PLOT column coupled to a mass spectrometer (GC–MS, Agilent GC 6890, Agilent MSD 5973N). After the GC–MS analysis, the gas stream was passed through two impinging bottles in series containing an aqueous solution of NaOH (1 M) for neutralization prior to its release in the ventilation system.

The conversion of dibromomethane, $X(CH_2Br_2)$, was calculated using Equation (1)

$$X(CH_2Br_2) = \frac{n(CH_2Br_2)_{in} - n(CH_2Br_2)_{out}}{n(CH_2Br_2)_{in}} \times 100\% \quad (1)$$

where $n(CH_2Br_2)_{in}$ and $n(CH_2Br_2)_{out}$ are the molar flows of CH_2Br_2 at the reactor inlet and outlet, respectively. The selectivity, $S(j)$, to product j (j: CH_3Br, CH_4) was calculated according to Equation (2)

$$S(j) = \frac{n(j)_{out}}{n(CH_2Br_2)_{in} - n(CH_2Br_2)_{out}} \times 100\% \quad (2)$$

where $n(j)_{out}$ is the molar flow of product j at the reactor outlet. The reaction rate, r, based on the platinum loading and expressed with

respect to the CH_3Br production or to the CH_2Br_2 consumption, were calculated using Equations (3) and (4), respectively

$$r = \frac{n(CH_2Br_2)_{in} \times X(CH_2Br_2) \times S(CH_3Br)}{100 \times 100 \times W_{cat} \times \omega_{Pt}} \ mol_{CH_3Br}\ h^{-1}\ mol_{Pt}^{-1} \quad (3)$$

$$r = \frac{n(CH_2Br_2)_{in} \times X(CH_2Br_2)}{100 \times W_{cat} \times \omega_{Pt}} \ mol_{CH_2Br_2}\ h^{-1}\ mol_{Pt}^{-1} \quad (4)$$

where W_{cat} is the weight of the catalyst and ω_{Pt} is the platinum loading determined by ICP-OES analysis (Table 2). The turnover frequency, *TOF*, was calculated using Equation (5),

$$TOF = \frac{n(CH_2Br_2)_{in} \times X(CH_2Br_2)}{100 \times W_{cat} \times \omega_{Pt} \times D_{Pt}} \ h^{-1} \quad (5)$$

where D_{Pt} is the platinum dispersion, determined by CO pulse chemisorption. A platinum dispersion of 100% was used for the SA-based catalysts. The error of the carbon balance, ε_C, in all catalytic tests was determined using Equation (6)

$$\varepsilon_C = \frac{n(CH_2Br_2)_{in} - n(CH_2Br_2)_{out} - n(j)_{out}}{n(CH_2Br_2)_{in}} \times 100\% \quad (6)$$

where $n(j)_{out}$ is the molar flow of product j (j: CH_3Br, CH_4) at the reactor outlet.

After the tests, the reactor was quenched to room temperature in He flow and the catalyst was retrieved for further characterization analyses. Evaluation of the dimensionless moduli based on the criteria of Carberry, Mears, and Weisz–Prater indicated that the catalytic tests were performed in the absence of mass and heat transfer limitations. Additionally, CH_2Br_2 hydrodebromination tests over Pt/NC-473 and Pt/AC-473 performed at variable flow rates and constant space velocity (F_T:W_{cat}) as well as by using catalyst particles of different sizes (d_p = 0.15–0.5 mm) at constant space velocity verified the absence of extra- and intraparticle mass transfer limitations, respectively (Figure S7, Supporting Information).

Computational Details: Density functional theory (DFT) on slab models representing the different systems was employed as implemented in the Vienna Ab initio Simulation Package (VASP 5.4.4).[40,41] Generalized gradient approximation with the Perdew–Burke–Ernzerhof (GGA-PBE)[42] functional was used to obtain the exchange-correlation energies with dispersion contributions introduced,[43,44] and spin polarization was allowed when needed. Core electrons were described by projector augmented waves (PAW),[45,46] while valence monoelectronic states were expanded in plane waves with cut-off energy of 450 eV. The Brillouin zone was sampled with a gamma-centered grid of 3 × 3 × 1 k-point grid.

Single atom catalysts were modeled by a one-layer 6 × 6 slab of graphitic carbon separated by 19 Å of vacuum. Defects in the carbon sheet were introduced by replacing some C- by N-atoms and saturating the valence (N-doped carbon) and/or adding oxygen as epoxides (AC), and the Pt atom was then placed on the cavity or coordinating the O atoms. For Pt nanoparticles, the lowest energy surface (111) in a p(3 × 3) supercell was used. The slab had four metal layers built from a bulk with an optimized lattice parameter of 2.6997 Å. Only the adsorbates and the top two layers were allowed to relax. The layers were interspaced along the *z*-direction with a vacuum space of at least 15 Å, applying a correction to the arising dipole. The Brillouin zone was sampled with a gamma centered grid of 5 × 5 × 1. For all the investigated systems the structures were relaxed using convergence criteria of 10^{-4} eV (0.03 eV $Å^{-1}$ for the metallic systems) and 10^{-5} eV for the ionic and electronic steps, respectively.

Transition states were located following the climbing image nudged elastic band procedure (CI–NEB).[47] Some of the transition states were obtained through the improved dimer method,[48,49] using the structures of the transition states found in similar defects as the initial geometry guess.[50] Transition states were confirmed by diagonalizing the numerical Hessian matrix obtained by displacements of ±0.02 Å. All structures presented in this work can be retrieved from the ioChem-BD database.[51,52]

Supporting Information

Supporting Information is available from the Wiley Online Library or from the author.

Acknowledgements

This work was supported by ETH research grants ETH-43 18-1 and ETH-40 17-1, and by a predoctoral grant of MINECO La Caixa-Severo Ochoa through the Severo Ochoa Excellence Accreditation 2014–2018 (SEV-2013-0319). The authors thank the Paul Scherrer Institute, PSI, and the Scientific Center for Optical and Electron Microscopy at the ETH Zurich, ScopeM, for access to their facilities. Dr. Frank Krumeich is acknowledged for performing microscopic analyses. The authors thank BSC-RES for providing generous computational resources.

Conflict of Interest

The authors declare no conflict of interest.

Keywords

carbon carriers, hydrodebromination, mechanism, nanoparticles, single atoms, speciation

[1] R. A. Sheldon, *Chem. Soc. Rev.* **2012**, *41*, 1437.
[2] A. T. Bell, *Science* **2003**, *299*, 1688.
[3] L. Liu, A. Corma, *Chem. Rev.* **2018**, *118*, 4981.
[4] X. Cui, W. Li, P. Ryabchuk, K. Junge, M. Beller, *Nat. Catal.* **2018**, *1*, 385.
[5] J. Liu, *ACS Catal.* **2017**, *7*, 34.
[6] G. Kyriakou, M. B. Boucher, A. D. Jewell, E. A. Lewis, T. J. Lawton, A. E. Baber, H. L. Tierney, M. Flytzani-Stephanopoulos, E. C. H. Sykes, *Science* **2012**, *335*, 1209.
[7] S. Mitchell, E. Vorobyeva, J. Pérez-Ramírez, *Angew. Chem., Int. Ed.* **2018**, *57*, 15316.
[8] J. M. Thomas, R. Raja, D. W. Lewis, *Angew. Chem., Int. Ed.* **2005**, *44*, 6456.
[9] J. M. Thomas, *Design and Applications of Single-Site Heterogeneous Catalysts*, World Scientific, London **2012**.
[10] A. Wang, J. Li, T. Zhang, *Nat. Rev. Chem.* **2018**, *2*, 65.
[11] H. Zhang, G. Liu, J. Ye, *Adv. Energy Mater.* **2018**, *8*, 1701343.
[12] C. Zhu, S. Fu, Q. Shi, D. Du, L. Y, *Angew. Chem., Int. Ed.* **2017**, *56*, 13944.
[13] C. Ye, D. Wang, Y. Li, *Chem. Commun.* **2020**, *56*, 7687.
[14] G. Vilé, D. Albani, M. Nachtegaal, Z. Chen, D. Dontsova, M. Antonietti, N. López, J. Pérez-Ramírez, *Angew. Chem., Int. Ed.* **2015**, *54*, 11265.

[15] R. Lin, D. Albani, E. Fako, S. K. Kaiser, O. V. Safonova, N. López, J. Pérez-Ramírez, *Angew. Chem., Int. Ed.* **2019**, *58*, 504.
[16] S. K. Kaiser, R. Lin, S. Mitchell, E. Fako, F. Krumeich, R. Hauert, O. V. Safonova, V. A. Kondratenko, E. V. Kondratenko, S. M. Collins, P. A. Midgley, N. López, J. Pérez-Ramírez, *Chem. Sci.* **2019**, *10*, 359.
[17] S. K. Kaiser, E. Fako, G. Manzocchi, F. Krumeich, R. Hauert, A. H. Clark, O. V. Safonova, N. López, J. Pérez-Ramírez, *Nat. Catal.* **2020**, *3*, 376.
[18] C. H. Bartholomew, R. J. Farrauto, *Fundamentals of Industrial Catalytic Processes*, John Wiley & Sons, New York **2011**.
[19] S. Nishimura, *Handbook of Heterogeneous Catalytic Hydrogenation for Organic Synthesis*, Wiley, New York **2001**.
[20] P. T. Witte, P. H. Berben, S. Boland, E. H. Boymans, D. Vogt, J. W. Geus, J. G. Donkervoort, *Top. Catal.* **2012**, *55*, 505.
[21] D. Astruc, *Nanoparticles and Catalysis*, Wiley-VCH, Weinheim **2008**.
[22] S. Schauermann, N. Nilius, S. Shaikhutdinov, H.-J. Freund, *Acc. Chem. Res.* **2013**, *46*, 1673.
[23] M. Sankar, N. Dimitratos, P. J. Miedziak, P. P. Wells, C. J. Kiely, G. J. Hutchings, *Chem. Soc. Rev.* **2012**, *41*, 8099.
[24] G. Vilé, D. Albani, N. Almora-Barrios, N. López, J. Pérez-Ramírez, *ChemCatChem* **2016**, *8*, 21.
[25] N. Semagina, L. Kiwi-Minsker, *Catal. Rev.: Sci. Eng.* **2009**, *51*,147.
[26] P. Mäki-Arvela, J. Hájek, T. Salmi, D. Y. Murzin, *Appl. Catal., A* **2005**, *292*, 1.
[27] A. J. McCue, J. A. Anderson, *Front. Chem. Sci. Eng.* **2015**, *9*, 142.
[28] E. McFarland, *Science* **2012**, *338*, 340.
[29] R. Lin, A. P. Amrute, J. Pérez-Ramírez, *Chem. Rev.* **2017**, *117*, 4182.
[30] K. Ding, A. R. Derk, A. Zhang, Z. Hu, P. Stoimenov, G. D. Stucky, H. Metiu, E. W. McFarland, *ACS Catal.* **2012**, *2*, 479.
[31] A. J. Saadun, S. Pablo-García, V. Paunovic, Q. Li, A. Sabadell-Rendón, K. Kleemann, F. Krumeich, N. López, J. Pérez-Ramírez, *ACS Catal.* **2020**, *10*, 6129.
[32] A. J. Saadun, G. Zichittella, V. Paunović, B. A. Markaide-Aiastui, S. Mitchell, J. Pérez-Ramírez, *ACS Catal.* **2020**, *10*, 528.
[33] M. Muhler, Z. Paál, R. Schlögl, *Appl. Surf. Sci.* **1991**, *47*, 281.
[34] G. Vilé, D. Baudouin, I. N. Remediakis, C. Copéret, N. López, J. Pérez-Ramírez, *ChemCatChem* **2013**, *5*, 3750.
[35] S. Kozuch, *Wiley Interdiscip. Rev.: Comput. Mol. Sci.* **2012**, *2*, 795.
[36] F. Abild-Petersen, J. Greeley, F. Studt, J. Rossmeisl, T. R. Munter, P. G. Moses, E. Skúlason, T. Bilgaard, J. K. Nørskov, *Phys. Rev. Lett.* **2007**, *99*, 016105.
[37] H. Au, N. Rubio, M. S. Shaffer, *Chem. Sci.* **2018**, *9*, 209.
[38] E. Papirer, R. Lacroix, J.-B. Donnet, G. Nanse, P. Fioux, *Carbon* **1994**, *32*, 1341.
[39] J. Chastain, *Handbook of X-Ray Photoelectron Spectroscopy*, Perkin-Elmer Corporation, Waltham, MA **1992**.
[40] G. Kresse, J. Fürthmuller, *Comput. Mater. Sci.* **1996**, *6*, 15.
[41] G. Kresse, J. Fürthmuller, *Phys. Rev. B* **1996**, *54*, 11169.
[42] J. P. Perdew, K. Burke, M. Ernzerhof, *Phys. Rev. Lett.* **1996**, *77*, 3865.
[43] S. Grimme, S. Ehrlich, L. Goerigk, *J. Comput. Chem.* **2011**, *32*, 1456.
[44] N. Almora-Barrios, G. Carchini, P. Błoński, N. López, *J. Chem. Theory Comput.* **2014**, *10*, 5002.
[45] G. Kresse, D. Joubert, *Phys. Rev. B* **1999**, *59*, 1758.
[46] P. E. Blöchl, *Phys. Rev. B* **1994**, *50*, 17953.
[47] G. Henkelman, H. Jónsson, *J. Chem. Phys.* **2000**, *113*, 9978.
[48] A. Heyden, *J. Chem. Phys.* **2005**, *123*, 224101.
[49] G. Henkelman, H. Jónsson, *J. Chem. Phys.* **1999**, *111*, 7010.
[50] S. Pablo-García, M. Álvarez-Moreno, N. López, *Int. J. Quantum Chem.* **2021**, *121*, e26382.
[51] A. Ruiz-Ferrando, *Pt Dehydrobromination Dataset*, https://doi.org/10.19061/iochem-bd-1-179 (accessed: November 2020)
[52] S. Pablo-García, CH_2Br_2 Dataset, **2020**, https://doi.org/10.19061/iochem-bd-1-150 (accessed: November 2020).